Original Paper

Synthesis of ZSM-22/SAPO-11 composite molecular sieve-based catalysts with small crystallites and superior n-alkane hydroisomerization performance

Xue-Man Wang [a], Cheng-Long Wen [b, **], Yu Fan [a, *]

[a] State Key Laboratory of Heavy Oil Processing, China University of Petroleum, Beijing, 102249, China
[b] Jiangsu Key Laboratory of Advanced Catalytic Materials and Technology, Advanced Catalysis and Green Manufacturing Collaborative Innovation Center, School of Petrochemical Engineering, Changzhou University, Changzhou, Jiangsu, 213164, China

A B S T R A C T

To improve oil quality, ZSM-22/SAPO-11 composite molecular sieves were synthesized by adding ZSM-22 into a synthetic gel of SAPO-11 for n-decane hydroisomerization. The mass ratios of ZSM-22/(ZSM-22+SAPO-11) in the composite molecular sieves were optimized and the optimal ZSM-22/SAPO-11 composite (ZS-9) was obtained. The electrostatic repulsions between the ZSM-22 precursors and the SAPO-11 crystalline nuclei produced small ZSM-22 and SAPO-11 crystallites in ZS-9, which increased the specific surface area and mesopore volume and thereby exposed more acid sites. In comparison with conventional SAPO-11, ZSM-22 and their mechanical mixture, ZS-9 with smaller crystallites and the optimal medium and strong Brønsted acid centers (MSBAC) content displayed a higher yield of branched C_{10} isomers (81.6%), lower cracking selectivity (11.9%) and excellent stability. The correlation between the i-C_{10} selectivity and the MSBAC density of molecular sieves indicated that the selectivity for branched C_{10} isomers first increased and then decreased with increasing MSBAC density on the molecular sieves, and the maximum selectivity (87.7%) occurred with a density of 9.6×10^{-2} μmol m^{-2}.

1. Introduction

n-Alkane hydroisomerization (AHI) is one of the most important catalytic processes in the petroleum industry. It converts n-alkanes into branched-alkanes, which plays significant roles in improving the gasoline octane number, reducing the diesel condensation point and enhancing the low-temperature fluidity of lubricant oils (Chi et al., 2013; Jaroszewska et al., 2019). In AHI, bifunctional catalysts composed of metal components and supports are utilized, in which the metal components catalyze (de)hydrogenation while the supports provide acid sites for the skeletal isomerizations (Jin et al., 2009; Zhan et al., 2022). Many studies have shown that the crystallite sizes and acidities of supports have significant effects on AHI. The supports with small crystallites have short residence times

for isomerized intermediates in their channels, which limits cracking side reactions in AHI (Oenema et al., 2020). Supports with few Brønsted acid centers (BAC) display low activities for AHI, while supports with excess BAC exhibit high cracking selectivity (Dai et al., 2022; Wei et al., 2022). SAPO-11 and ZSM-22 molecular sieves with one-dimensional straight channels are widely used as catalyst supports for AHI due to their excellent shape selectivity (Claude and Martens, 2000; Lyu et al., 2020). However, conventional SAPO-11 and ZSM-22 have large crystallites, which restrain effective diffusion of isomerized intermediates and enhance cracking side reactions, thereby resulting in low isomer selectivity. Furthermore, conventional SAPO-11 has a weak acid strength and few BAC, which results in inferior n-alkane conversion (Liu et al., 2020; Wen et al., 2020; Yu et al., 2021). Compared with SAPO-11, conventional ZSM-22 possesses stronger acid sites and more BAC, thereby generating high n-alkane conversion, but its excess BAC enhance the cracking side reactions (Liu et al., 2015; Feng et al., 2019; Zhai et al., 2022).

Composite molecular sieves integrate the merits of individual molecular sieves and make up for the deficiencies of single

molecular sieves through coordination of different molecular sieves (Qin et al., 2011; Duan et al., 2013; Wang et al., 2018). Zhang et al. (2019) first treated a Y molecular sieve with different levels of alkali treatment, and then Y/MCM-41 composite molecular sieves with different crystallites were obtained by growing mesoporous MCM-41 on the external surface of Y. The n-dodecane hydroisomerization results showed that Y/MCM-41 with small crystallites presented a higher isomer yield than Y alone. Zhu et al. (2014) synthesized a SAPO-11/Beta composite molecular sieve using a Beta molecular sieve as the silicon source. The SAPO-11/Beta composite presented a higher isomer yield in n-dodecane hydroisomerization than SAPO-11, Beta and their mechanical mixture due to its optimal pore structure and acidity. Thus far, synthesis of the ZSM-22/SAPO-11 composite molecular sieve and its application in AHI have not been reported.

Herein, novel ZSM-22/SAPO-11 composite molecular sieves with different crystallites and different MSBAC were synthesized by incorporating different amounts of ZSM-22 into the synthetic gel of SAPO-11, and the effects of ZSM-22/SAPO-11 ratios in the composite on the physicochemical properties and n-C_{10} hydroisomerization performance were investigated. Compared with conventional SAPO-11, conventional ZSM-22 and their mechanical mixture, the advantages of the ZSM-22/SAPO-11 composite in n-C_{10} hydroisomerization were clarified. Additionally, the relationship between the MSBAC densities of different acidic supports and the selectivity for branched C_{10} isomers was quantitatively revealed.

2. Experimental

2.1. Preparation of supports

2.1.1. Synthesis of conventional SAPO-11

Conventional SAPO-11 was synthesized by following the method reported in the literature (Wen et al., 2021). First, 8.1 g of pseudoboehmite (Al_2O_3, 73.0 wt%; Shandong Aluminum Plant) was added to a mixture of 12.2 g of phosphoric acid (H_3PO_4, 85 wt%; Aladdin) and 40.0 g of deionized (DI) water and stirred for 3 h. Subsequently, 4.7 g of tetraethoxysilane ($C_8H_{20}O_4Si$, 99.0 wt%; Aladdin) and 6.8 g of di-n-propylamine ($C_6H_{15}N$, 99.5 wt%; Aladdin) were added to the above solution sequentially and stirred for 3 h to obtain a gel with the molar compositions of 40.0 H_2O:0.4 SiO_2:1.0 Al_2O_3:1.9 H_3PO_4:1.2 $C_6H_{15}N$. Afterward, the gel was loaded into a 100 mL autoclave and heated at 200 °C for 24 h. Finally, the resulting product was washed with DI water, dried at 120 °C for 12 h and calcined at 600 °C for 6 h to yield SAPO-11, which was named C-S.

2.1.2. Synthesis of conventional ZSM-22

Conventional ZSM-22 was synthesized by the procedures described in the literature (Feng et al., 2019). First, 0.4 g of aluminum sulfate octadecahydrate ($Al_2(SO_4)_3 \cdot 18H_2O$, 98.0 wt%; Aladdin) was dissolved in 40.0 g of DI water, followed by addition of 1.0 g of potassium hydroxide (KOH, 95.0 wt%; Aladdin) and stirring for 0.5 h. Subsequently, 2.6 g of 1,6-hexamethylenediamine ($C_6H_{16}N_2$, 95.0 wt%; Aladdin) and 11.1 g of silica sol (SiO_2, 30.0 wt%; Guangzhou Huixin Company) were added sequentially to the above solution and stirred for 5 h to afford an initial gel with the molar compositions of 40.0 H_2O:1.0 SiO_2:0.01 Al_2O_3:0.3 KOH:0.4 $C_6H_{16}N_2$. Afterward, the gel was crystallized dynamically (60 rpm) at 160 °C for 72 h, and K-ZSM-22 was obtained after the resulting product was filtered, heated at 120 °C for 12 h and calcined at 600 °C for 6 h. Finally, K-ZSM-22 was treated with ammonium chloride solution (NH_4Cl, 99.5%; Aladdin) three times at 80 °C and then washed, dried at 120 °C for 12 h and calcined at 600 °C for 6 h to afford ZSM-22, which was named C-Z.
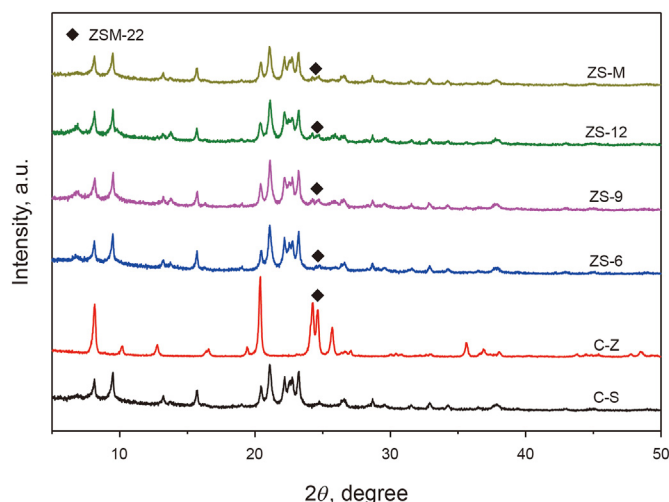

Fig. 1. XRD patterns of C-S, C-Z, ZS-6, ZS-9, ZS-12 and ZS-M.

2.1.3. Synthesis of the ZSM-22/SAPO-11 composite

The synthetic procedures for preparation of the ZSM-22/SAPO-11 composite were as follows. First, the ZSM-22 precursor was prepared by following the same procedures used for C-Z, except that the crystallization time was reduced to 48 h and the post-treatments (such as ammonium exchange and calcination) were omitted. Subsequently, K-ZSM-22/SAPO-11 composites were synthesized via the same procedures used for C-S, except that different amounts of ZSM-22 precursors were added and stirred for 2 h before adding the DPA. After the K-ZSM-22/SAPO-11 composites were exchanged with NH_4Cl solution three times, washed, dried at 120 °C for 12 h and calcined at 600 °C for 6 h, ZSM-22/SAPO-11 composites with different ZSM-22/SAPO-11 ratios were obtained, which were denoted ZS-x (x = 6, 9 and 12, corresponding to the ZSM-22 mass fractions of 6.5%, 9.4% and 12.2% contained in ZSM-22/SAPO-11, respectively).

2.1.4. Synthesis of the ZSM-22 and SAPO-11 mechanical mixture

The mechanical mixture of ZSM-22 and SAPO-11 was obtained after ZSM-22 and SAPO-11 were fully ground in accordance with the ZSM-22/SAPO-11 ratio in ZS-9, and it was named ZS-M.

2.2. Preparation of catalysts

The catalysts containing 0.5 wt% Pt were prepared through incipient wetness impregnation. First, the above synthesized supports were pressed and crushed into particles with 20–40 mesh. Afterward, a chloroplatinic acid solution ($H_2PtCl_6 \cdot 6H_2O$, 37.0 wt%; Aladdin) was added dropwise to the particles and then stirred thoroughly. Finally, the catalyst precursors were placed into an oven at 120 °C for 6 h, calcined at 450 °C for 4 h and then sieved again to obtain Pt-supported molecular sieve-based catalysts, which were named Pt/C-S, Pt/C-Z, Pt/ZS-6, Pt/ZS-9, Pt/ZS-12 and Pt/ZS-M.

2.3. Characterization

X-ray diffraction (XRD) patterns were determined with a D8 ADVANCE X-ray diffractometer equipped with Cu Kα radiation, and the scanning speed and range were 4°/min and 5−50°, respectively. Scanning electron microscopy (SEM) images were obtained with an SU8010 instrument. The zeta potentials of the samples were determined with a Zetasizer Nano ZS instrument. Fourier transform
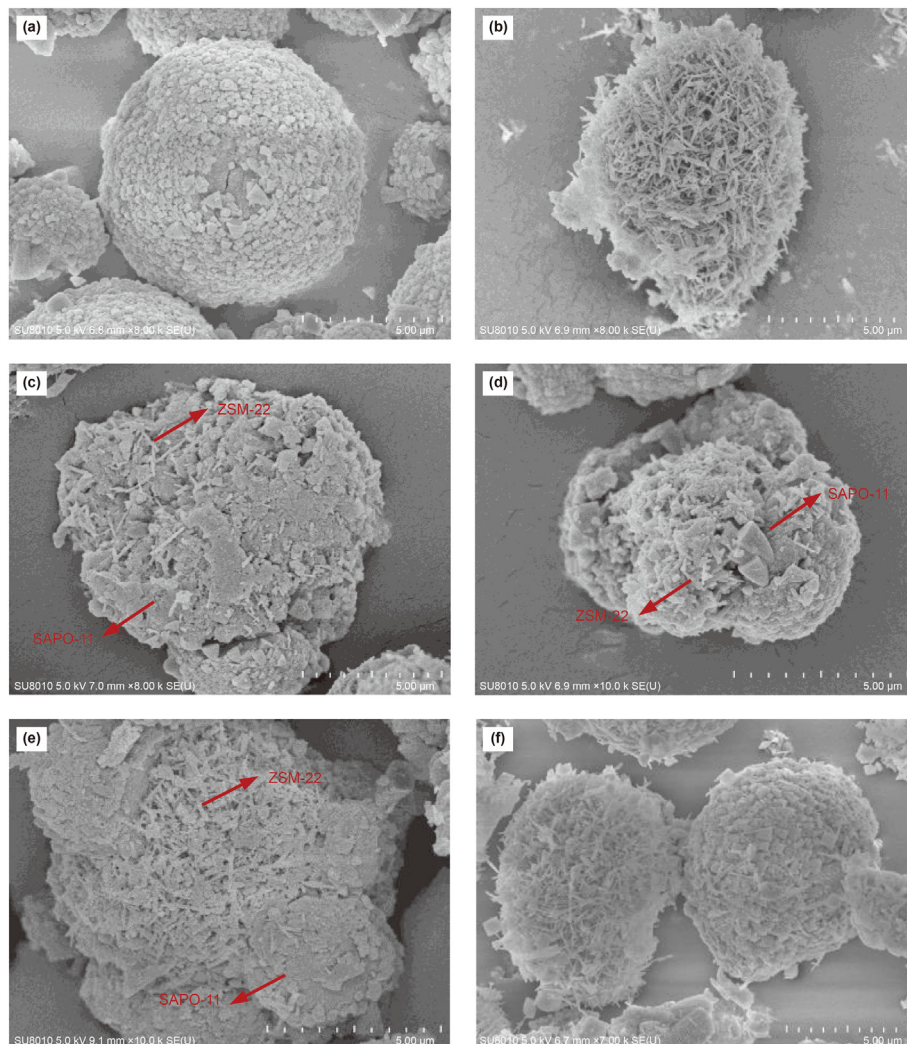
Fig. 2. SEM images of C-S (**a**), C-Z (**b**), ZS-6 (**c**), ZS-9 (**d**), ZS-12 (**e**) and ZS-M (**f**).

infrared (FT-IR) spectra were obtained with a Spectrum GX instrument. Before the measurement, the sample and potassium bromide power were mixed evenly at a mass ratio of 1:100 and then pressed into a disk with a diameter of 13 mm. N_2 adsorption-desorption experiments were performed on an ASAP 2420 adsorption apparatus. A total of 0.1 g of sample was put into the apparatus and treated at 350 °C for 6 h under vacuum, and then physical adsorption was conducted at −196 °C with N_2 as the adsorbent. The specific surface area and pore volume were calculated with the Brunauer-Emmett-Teller (BET) method and t-plot method, respectively (Barrett et al., 1951; Lippens and Boer, 1965). Transmission electron microscopy (TEM) images were obtained with an FEI Tecnai G2 F20 microscope. The samples were ground in a mortar and dispersed with ethanol before measurement.

The elemental compositions of the samples were obtained on a ZSX-100e X-ray fluorescence spectroscopy (XRF). The acid contents of the samples were determined by the NH_3 temperature programmed desorption (NH_3-TPD) experiments. Pyridine infrared (Py-IR) spectra were obtained on a Nicolet-750 infrared spectrometer, and the details are as follows. A total of 0.02 g of sample was pressed into a 13 mm disk and then pretreated at 400 °C for 1 h. Afterward, adsorption of pyridine was performed at 30 °C, and then desorption of pyridine was carried out at 200 °C and then 350 °C.

Finally, spectra were recorded after the temperature cooled to 30 °C. The Pt dispersions of all catalysts were analyzed by H_2 chemical adsorption, which was carried out on an Auto Chem II 2920 adsorption apparatus.

2.4. Evaluation of catalytic performance

The n-C_{10} hydroisomerization capabilities of the catalysts were evaluated in a microreactor. The catalysts were reduced at 400 °C and pressurized under 2.0 MPa H_2 for 4 h before reaction. After the reduction reaction was finished, n-C_{10} was pumped into the microreactor at a temperature of 270−390 °C, a pressure of 2.0 MPa, a weight hourly space velocity of 3.0 h^{-1} and a H_2 to n-C_{10} volumetric ratio of 400.

The compositions of the hydroisomerization products were determined with a Trace 1310 mass spectrometer, and the concentrations of the products were determined with an SP3420 gas chromatograph with a HP-PONA column. The n-C_{10} conversion, selectivity for branched C_{10} isomers (i-C_{10} selectivity), yield of branched C_{10} isomers (i-C_{10} yield) and cracking selectivity were obtained with the following formulas:
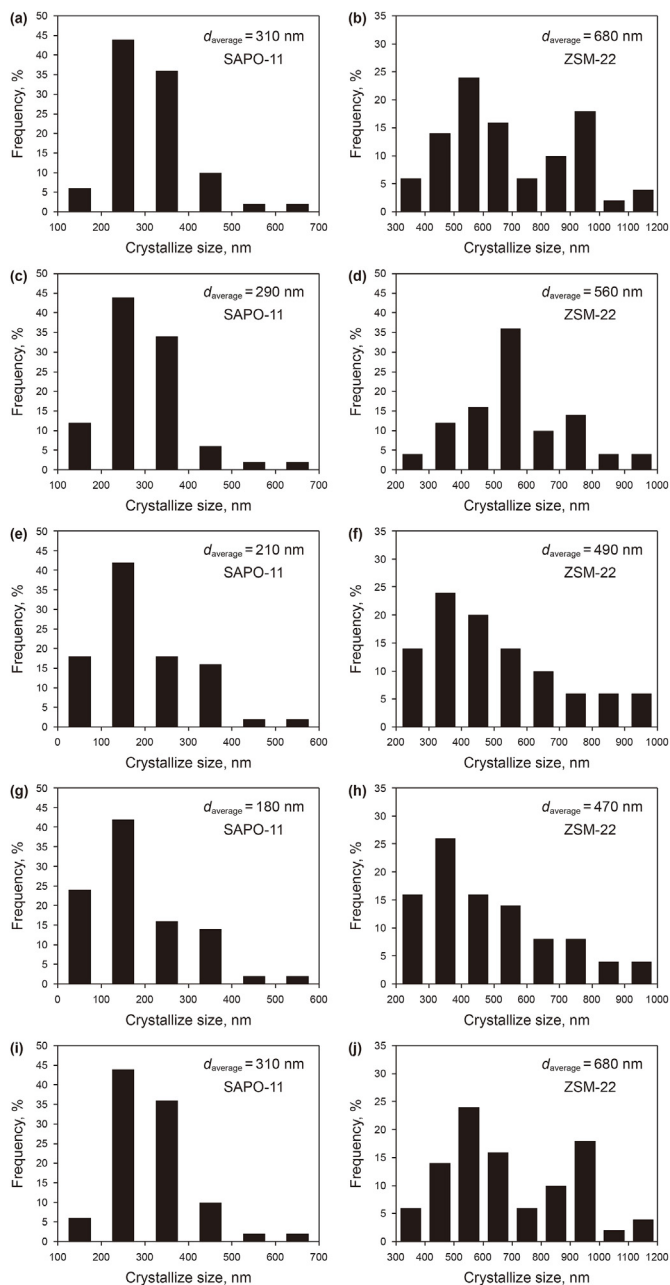
Fig. 3. Crystallite size distributions of C-S (**a**), C-Z (**b**), ZS-6 (**c**, **d**), ZS-9 (**e**, **f**), ZS-12 (**g**, **h**) and ZS-M (**i**, **j**).
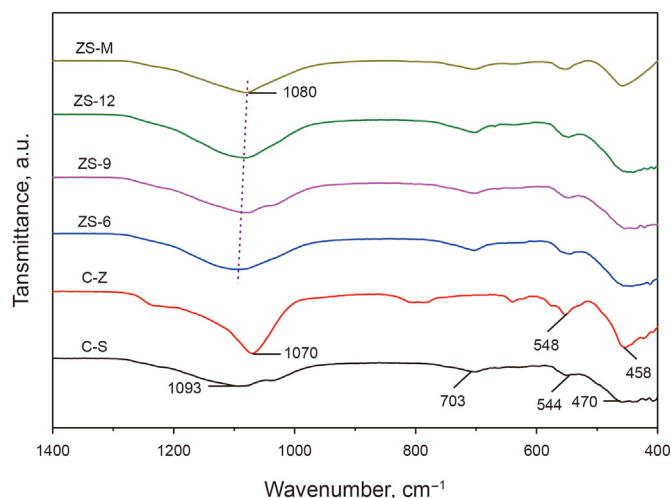

Fig. 4. FT-IR spectra of C-S, C-Z, ZS-6, ZS-9, ZS-12 and ZS-M.

$$\text{Cracking selectivity} = \frac{C_c}{C_r - C_p} \times 100\% \qquad (4)$$

where C_r and C_p are the concentrations of n-C_{10} in the feedstock and products, respectively, and C_i and C_c are the concentrations of branched C_{10} isomers (i-C_{10}) and cracked products in the products, respectively.

The turnover frequency (TOF) of a catalyst was calculated with the following formula (Guo et al., 2012):

$$TOF = \frac{n}{C_{MSBAC}} \qquad (5)$$

where n is the number of reacted n-C_{10} mol per unit gram of catalyst per second (mol g^{-1} s^{-1}) and C_{MSBAC} is the MSBAC content per gram of catalyst (mol g^{-1}).

To better illustrate the effects of support acidity on the n-C_{10} hydroisomerization performance, the MSBAC density was defined by the ratio of the MSBAC content to the specific surface area of the support:

$$\text{MSBAC density} = \frac{C_{MSBAC}}{S_{BET}} \qquad (6)$$

3. Results and discussion

3.1. XRD

The XRD patterns of the samples are presented in Fig. 1. ZS-x and ZS-M with high SAPO-11 crystallinities (Table S1) showed the characteristic peaks of SAPO-11 ($2\theta = 9.4, 13.1, 15.6,$ and $22.1-23.3°$) and ZSM-22 ($2\theta = 24.2, 24.6$ and $25.7°$) (Lyu et al., 2019; Wang et al., 2019), indicating the presence of both SAPO-11 and ZSM-22 in ZS-x and ZS-M.

3.2. SEM

The SEM images of the samples are displayed in Fig. 2. C-S presented spherical particles composed of flaked crystallites (Fig. 2a). C-Z showed nest-like particles made up of acicular
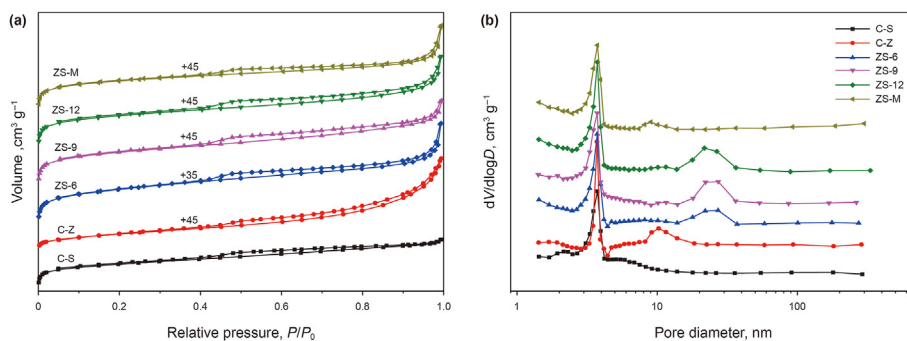
$$\text{Conversion} = \frac{C_r - C_p}{C_r} \times 100\% \qquad (1)$$

$$\text{i-}C_{10} \text{ selectivity} = \frac{C_i}{C_r - C_p} \times 100\% \qquad (2)$$

$$\text{i-}C_{10} \text{ yield} = \frac{C_i}{C_r} \times 100\% \qquad (3)$$

Fig. 5. N$_2$ absorption-desorption isotherms (**a**) and pore size distributions (**b**) for C-S, C-Z, ZS-6, ZS-9, ZS-12 and ZS-M.

Table 1
Textural properties of C-S, C-Z, ZS-6, ZS-9, ZS-12 and ZS-M.

Sample	S_{BET}, m^2 g^{-1}	$V_{micropore}$, cm^3 g^{-1}	$V_{mesopore}$, cm^3 g^{-1}
C-S	215	0.05	0.06
C-Z	235	0.06	0.11
ZS-6	221	0.06	0.13
ZS-9	239	0.06	0.16
ZS-12	243	0.06	0.17
ZS-M	219	0.06	0.08
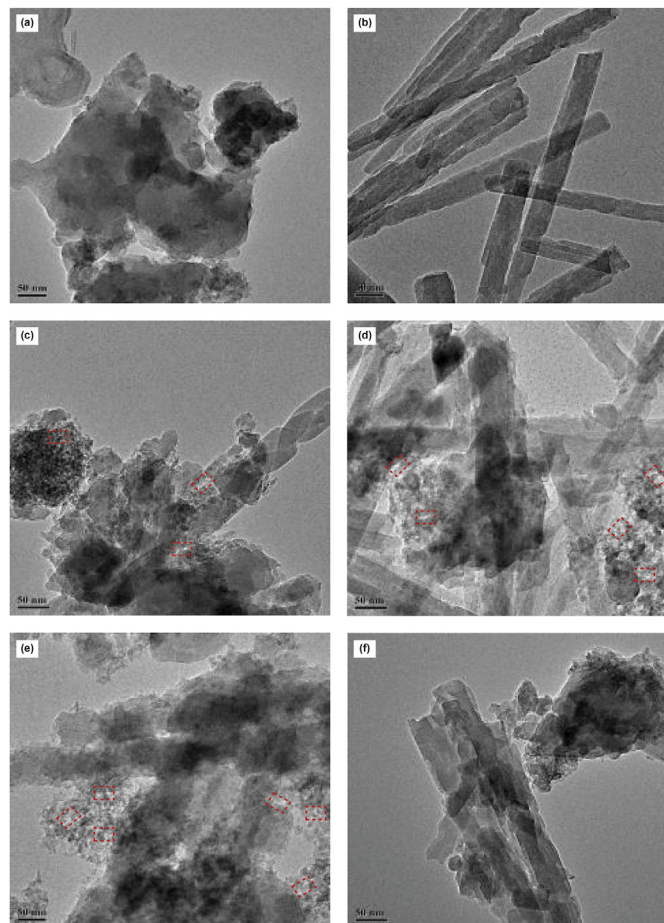
Fig. 6. TEM images of C-S (**a**), C-Z (**b**), ZS-6 (**c**) ZS-9 (**d**), ZS-12 (**e**) and ZS-M (**f**).

crystallites (Fig. 2b). As for ZS-*x*, the acicular crystallites of ZSM-22 were dispersed on the SAPO-11 particles (Fig. 2c−e), indicating the composite structure in ZS-*x*. Additionally, the number of acicular ZSM-22 crystallites on the SAPO-11 particles in ZS-*x* increased along with the increasing ZSM-22 amounts. As for ZS-M (Fig. 2f), mechanically mixed SAPO-11 and ZSM-22 were separated completely from each other.

The crystallite size distributions of the samples according to statistical analyses with at least 500 crystallites are displayed in Fig. 3. The average crystallite sizes of C-S and C-Z were 310 and 680 nm, respectively (Fig. 3a and b), and those of SAPO-11 and ZSM-22 in ZS-6, ZS-9 and ZS-12 were 290 and 560 nm (Fig. 3c and d), 210 and 490 nm (Fig. 3e and f), 180 and 470 nm (Fig. 3g and h), respectively. Compared with C-S and C-Z, the ZS-*x* composites had smaller SAPO-11 or ZSM-22 crystallites. This was because the SAPO-11 or ZSM-22 crystalline nuclei were easily polymerized to form large crystallites during the synthesis of C-S or C-Z (Fig. 3a and b). The zeta potential of the ZSM-22 precursor was −7.83 mV in the synthetic solution of ZS-*x* (pH = 6.0), and the SAPO-11 crystal nuclei were negatively charged (Wen et al., 2021). Consequently, the electrostatic repulsions between SAPO-11 crystalline nuclei and ZSM-22 precursors favored good dispersion, and therefore ZS-*x* exhibited smaller SAPO-11 and ZSM-22 crystallites than C-S and C-Z. For ZS-*x*, a small amount of ZSM-22 led to weak electrostatic repulsions between the ZSM-22 precursors and the SAPO-11 crystalline nuclei, which resulted in relatively large SAPO-11 and ZSM-22 crystallites in ZS-6 (Fig. 3c and d). As the ZSM-22 amount added to ZS-*x* was increased, the electrostatic repulsions between the ZSM-22 precursor and the SAPO-11 crystalline nuclei were enhanced, which promoted good dispersion. Consequently, ZS-9 and ZS-12 showed small SAPO-11 and ZSM-22 crystallites (Fig. 3e−h). ZS-M comprised mechanically mixed SAPO-11 and ZSM-22, in which the crystallite sizes of SAPO-11 and ZSM-22 were 310 and 680 nm, respectively (Fig. 3i and j).

3.3. FT-IR

Fig. 4 displays the FT-IR spectra of the samples. The bands at 1093 and 703 cm^{-1} were assigned to the asymmetric and symmetric stretching vibrations of T-O-T in SAPO-11, respectively, and the bands at 544 and 470 cm^{-1} were for deformation vibrations of the six-membered rings and the four-membered rings in SAPO-11, respectively (Fan et al., 2006; Lyu et al., 2018). The bands at 1070, 548 and 458 cm^{-1} were ascribed to the asymmetric stretching vibrations of T-O-T, vibrations of the double five-membered rings and the bending vibrations of internal TO$_4$ tetrahedra in ZSM-22, respectively (Gollakota et al., 2020). The FT-IR results showed that
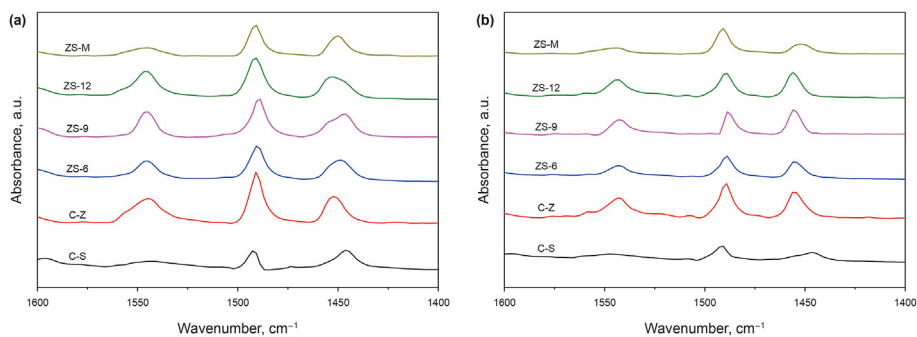
Fig. 7. Py-IR spectra of C-S, C-Z, ZS-6, ZS-9, ZS-12 and ZS-M at 200 °C (**a**) and 350 °C (**b**).

Table 2
B and L acidities of C-S, C-Z, ZS-6, ZS-9, ZS-12 and ZS-M.

Sample	200 °C Acidity, μmol/g		350 °C Acidity, μmol/g	
	B	L	B	L
C-S	25.1	31.2	11.3	12.4
C-Z	86.6	34.9	37.8	26.0
ZS-6	42.8	40.4	15.2	17.4
ZS-9	55.2	47.2	23.0	19.1
ZS-12	69.4	46.8	28.4	23.0
ZS-M	28.7	30.5	12.5	11.6

ZS-*x* and ZS-M consisted of SAPO-11 and ZSM-22, which was consistent with the XRD results. Additionally, the asymmetric stretching vibrations of ZS-*x* were shifted toward higher energies in comparison to that of ZS-M at 1080 cm^{-1} (dotted line), which was attributed to the interactions between ZSM-22 and SAPO-11 in ZS-*x* (Zheng et al., 2015). The asymmetric stretching vibrations of ZS-*x* were shifted toward lower energies upon addition of increasing ZSM-22 amounts, which was due to the T-O-T asymmetric stretching vibration in ZSM-22 (1070 cm^{-1}); this was located at a lower energy relative to that of SAPO-11 (1093 cm^{-1}).

3.4. N$_2$ adsorption-desorption

Fig. 5a shows the N$_2$ adsorption-desorption isotherms for the samples. All samples presented distinct hysteresis loops within the relative pressure range of 0.4–0.9, indicating that they all contained mesopores. Fig. 5b displays the pore size distributions of the samples. The peak seen at 3.8 nm for all samples was attributed to the tensile strength effect (Danilina et al., 2010). Compared with C-S, C-Z and ZS-M, the ZS-*x* composites exhibited broad peaks at 5–50 nm with higher intensities, indicating the presence of more mesopores.

The textural properties of the samples are displayed in Table 1. All samples exhibited almost identical micropore volumes but different mesopore volumes. The ZS-*x* composites had larger mesopore volumes than C-S, C-Z and ZS-M. With the addition of increasing ZSM-22 amounts, the S_{BET} and mesopore volumes of ZS-*x* rose because the SAPO-11 and ZSM-22 crystallite sizes in ZS-*x* gradually decreased, and small crystallites improved the pore structures of molecular sieves (Wen et al., 2021). In addition, ZS-9 had a larger S_{BET} than ZS-M because of the smaller ZSM-22 and SAPO-11 crystallites in ZS-9 compared to those in ZS-M.
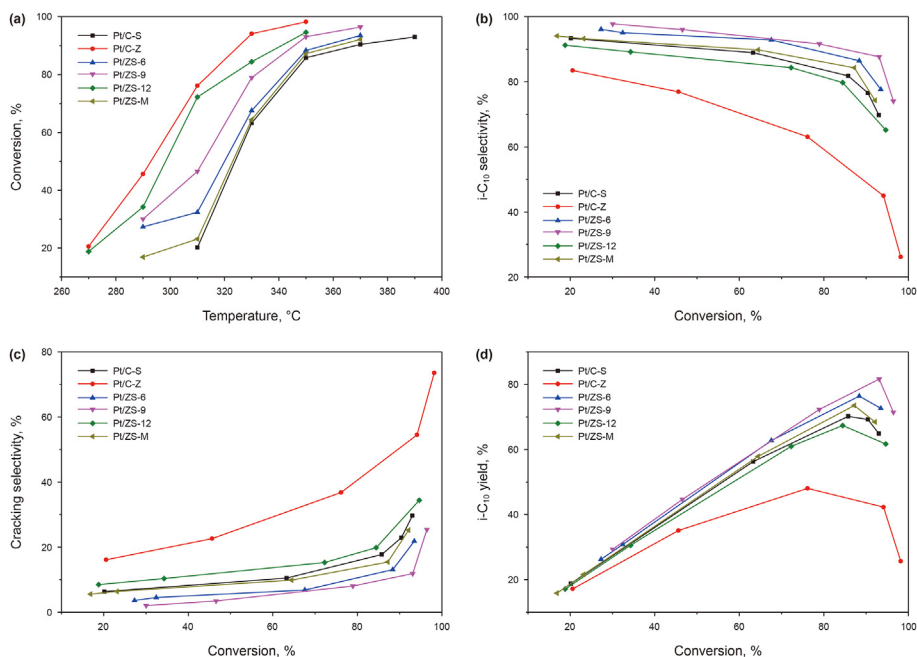

Fig. 8. n-C$_{10}$ conversion versus temperature (**a**), and i-C$_{10}$ selectivity (**b**), cracking selectivity (**c**) and i-C$_{10}$ yield (**d**) versus n-C$_{10}$ conversion for Pt/C-S, Pt/C-Z, Pt/ZS-6, Pt/ZS-9, Pt/ZS-12 and Pt/ZS-M.

3.5. TEM

The TEM images of the samples are shown in Fig. 6. The ZS-*x* (Fig. 6c–e) composites had more light areas (marked with red borders) than C-S and C-Z (Fig. 6a and b), indicating the presence of more mesopores in ZS-*x*. Compared with ZS-*x*, ZS-M contained fewer mesopores (Fig. 6f). The TEM results were consistent with the N_2 adsorption-desorption results described above.

3.6. Py-IR

The Py-IR spectra of the samples are shown in Fig. 7. All samples presented peaks at 1540, 1490 and 1450 cm^{-1}, which were ascribed to B acid centers, B + L acid centers and L acid centers, respectively (Parry, 1963; Pieterse et al., 1999). The total, medium and strong B/L acid centers of the samples were calculated on the basis of Py-IR spectra obtained after treatment at 200 and 350 °C, respectively (Zhang et al., 2008), and the results are shown in Table 2. The MSBAC of acidic supports provide the active sites for skeletal isomerization in AHI (Zhang et al., 2018). The MSBAC content decreased in the order C-Z (37.8 μmol/g) > ZS-12 (28.4 μmol/g) > ZS-9 (23.0 μmol/g) > ZS-6 (15.2 μmol/g) > ZS-M (12.5 μmol/g) > C-S (11.3 μmol/g), which was consistent with the NH_3-TPD results (Fig. S1). The MSBAC content in ZS-*x* increased gradually with increasing ZSM-22 amounts added. Additionally, although ZS-9 and ZS-M had the same composition (Table S1), ZS-9 contained more MSBAC contents than ZS-M. This was because ZS-9 had smaller crystallites than ZS-M, which increased the specific surface area and mesopore volume (Table 1) and thereby exposed more acid sites in ZS-9 compared to ZS-M (Zhou et al., 2011; Hoang et al., 2017; Hao et al., 2021).

3.7. Hydroisomerization performance

The n-C_{10} hydroisomerization reactions over the prepared catalysts were evaluated, and the results are displayed in Fig. 8. The n-C_{10} conversions for all catalysts increased with increasing temperature and decreased in the order Pt/C-Z > Pt/ZS-12 > Pt/ZS-9 > Pt/ZS-6 > Pt/ZS-M > Pt/C-S for the same temperature (Fig. 8a). As the n-C_{10} conversion increased, the i-C_{10} selectivities for all catalysts decreased, while the cracking selectivity increased (Fig. 8b and c). At the same n-C_{10} conversion, the i-C_{10} selectivity increased in the order Pt/C-Z < Pt/ZS-12 < Pt/C-S < Pt/ZS-M < Pt/ZS-6 < Pt/ZS-9, while the cracking selectivity exhibited the opposite order. The i-C_{10} yields for all catalysts first increased and then decreased with increasing n-C_{10} conversion, and they decreased in the order Pt/ZS-9 > Pt/ZS-6 > Pt/ZS-M > Pt/C-S > Pt/ZS-12 > Pt/C-Z for the same n-C_{10} conversion (Fig. 8d). Additionally, the maximum i-C_{10} yields for Pt/ZS-9, Pt/ZS-6, Pt/ZS-M, Pt/C-S, Pt/ZS-12 and Pt/C-Z were 81.6%, 76.4%, 73.5%, 70.2%, 67.4% and 48.0%, respectively.

The results of n-C_{10} hydroisomerizations over Pt/C-S, Pt/C-Z, Pt/ZS-9 and Pt/ZS-M are presented in Table 3. At a n-C_{10} conversion of approximately 93%, the i-C_{10} selectivity increased in the order Pt/C-Z (45.0%) < Pt/C-S (69.8%) < Pt/ZS-M (74.3%) < Pt/ZS-9 (87.7%), and the cracking selectivity decreased in the order Pt/C-Z (54.5%) > Pt/C-S (29.6%) > Pt/ZS-M (25.2%) > Pt/ZS-9 (11.9%). Furthermore, the TOF of Pt/ZS-9 was 30.7 × 10^{-1} s^{-1} at a n-C_{10} conversion of approximately 20%, which was higher than those of Pt/C-S (25.9 × 10^{-1} s^{-1}), Pt/C-Z (23.2 × 10^{-1} s^{-1}) and Pt/ZS-M (26.5 × 10^{-1} s^{-1}).

The n-C_{10} hydroisomerization results for these catalysts are explained as follows. The Pt loadings of these catalysts were all 0.5 wt%, which satisfied the requirement for hydrogenation-dehydrogenation in AHI (Wen et al., 2019). The TEM images and Pt size distributions for these catalysts are presented in Fig. 9. The

Table 3
Results of n-C_{10} hydroisomerizations over Pt/C-S, Pt/C-Z, Pt/ZS-9 and Pt/ZS-M.

TOF[a] (10^{-1} s^{-1})	Pt/C-S	Pt/C-Z	Pt/ZS-9	Pt/ZS-M
	25.9	23.2	30.7	26.5
i-C_{10} selectivity, %	69.8	45.0	87.7	74.3
S[b], %				
2-MC9	8.0	6.0	11.3	9.1
3-MC9	12.4	8.9	17.2	13.6
4-MC9	5.7	3.7	10.5	7.0
5-MC9	14.9	9.3	19.5	13.9
3-EC8	2.5	0.7	1.8	3.0
4-EC8	4.0	2.5	4.6	6.2
2,5-DMC8	5.1	3.3	5.2	5.3
2,6-DMC8	6.0	3.4	5.3	5.7
2,7-DMC8	3.2	2.1	3.5	3.6
3,3-DMC8	0.1	0.1	0.2	0.1
3,5-DMC8	0.1	0.1	0.2	0.2
3,6-DMC8	2.9	1.6	2.5	2.4
4,4-DMC8	4.4	2.9	4.9	3.6
4,5-DMC8	0.3	0.3	0.7	0.5
2-M-3-EC7	0.2	0.1	0.3	0.1
Others, %	0.6	0.5	0.4	0.5
Cracking selectivity, %	29.6	54.5	11.9	25.2

[a] Obtained at 350 °C, 2.0 MPa, a $v(H_2)/v$(n-C_{10}) of 400 and a n-C_{10} conversion of approximately 20%.
[b] S represents product selectivity.

average Pt particle sizes in these catalysts were almost identical at approximately 4.4 nm, and the Pt dispersions in these catalysts were also nearly identical at 54%–55%. As a result, the n-C_{10} hydroisomerization performance was chiefly affected by the physicochemical properties of the acidic supports (Wen et al., 2021).

The n-C_{10} hydroisomerization over these catalysts followed a bifunctional reaction mechanism (Zhang et al., 2019; Yu et al., 2020). First, n-C_{10} was transformed to n-decene after dehydrogenation at Pt sites. Then, the n-decene diffused into the channels of the acidic supports and underwent skeletal rearrangement at the MSBAC to produce i-C_{10} intermediates. Finally, the i-C_{10} intermediates were hydrogenated at Pt sites to afford the i-C_{10} products.

As the amount of ZSM-22 was increased, the n-C_{10} conversion for Pt/ZS-*x* gradually increased at the same temperature, and the i-C_{10} selectivity first increased and then decreased for the same n-C_{10} conversion. When the mass fraction of ZSM-22 in the ZSM-22/SAPO-11 composites was 9.4%, the corresponding Pt/ZS-9 catalyst displayed the highest i-C_{10} selectivity (87.7%) and i-C_{10} yield (81.6%) and the lowest cracking selectivity (11.9%). These results are explained as follows. Compared with ZS-6 (15.2 μmol/g), ZS-9 had more MSBAC content (23.0 μmol/g), which provided more active sites for n-C_{10} skeletal isomerizations and thereby improved the n-C_{10} conversion. Additionally, ZS-9 had smaller ZSM-22 (490 nm) and SAPO-11 (210 nm) crystallites than ZS-6, which favored diffusion of i-C_{10} intermediates and thereby reduced the extent of cracking side reactions. Although ZS-12 had relatively smaller crystallite sizes for ZSM-22 (470 nm) and SAPO-11 (180 nm) than ZS-9 (490 and 210 nm), its excess MSBAC content affected the cracking side-reactions and resulted in lower i-C_{10} selectivity and i-C_{10} yield but higher cracking selectivity over Pt/ZS-12 than over Pt/ZS-9 (Wen et al., 2020).

Among these catalysts, Pt/C-S presented the lowest n-C_{10} conversion, while Pt/C-Z showed the highest n-C_{10} conversion and cracking selectivity and the lowest i-C_{10} selectivity and i-C_{10} yield at the same n-C_{10} conversion. The Py-IR results showed that C-S had the lowest MSBAC content (11.3 μmol/g) among these samples and provided the fewest active sites for n-C_{10} skeletal isomerizations. As a consequence, the corresponding Pt/C-S catalyst showed the
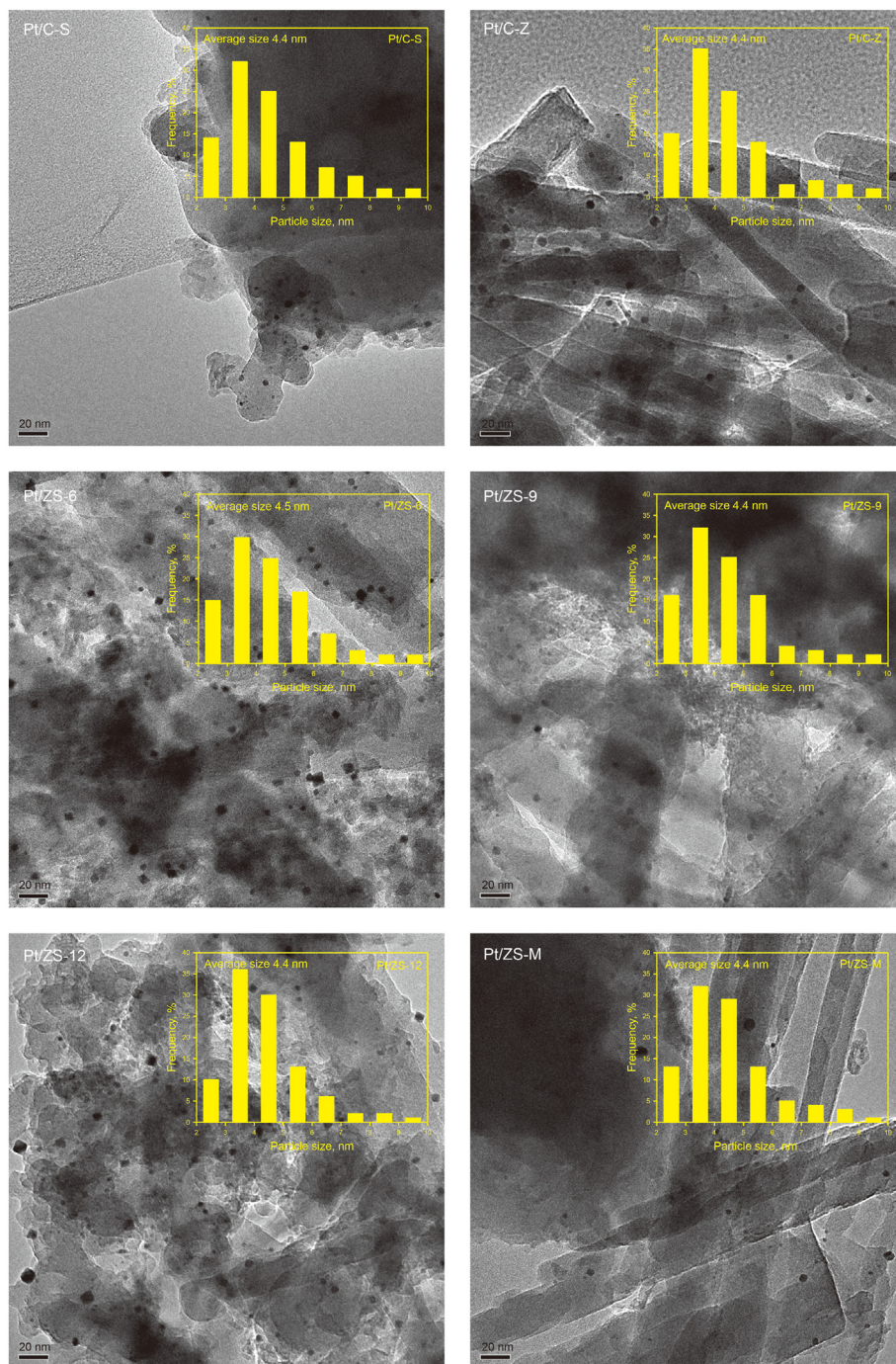
Fig. 9. TEM images and Pt size distributions for Pt/C-S, Pt/C-Z, Pt/ZS-6, Pt/ZS-9, Pt/ZS-12 and Pt/ZS-M.

lowest n-C_{10} conversion (Deldari, 2005). C–Z, with the largest MSBAC content (37.8 μmol/g), provided the greatest number of acid sites for n-C_{10} hydroisomerization, which resulted in the highest n-C_{10} conversion. However, the excess MSBAC content in C–Z exacerbated the cracking side reactions (Buchanan et al., 1996), and the large crystallites (680 nm) of C–Z led to long residence times in its channels for i-C_{10} intermediates. As a result, the i-C_{10} intermediates were easily cracked, giving Pt/C-Z the highest cracking selectivity and the lowest i-C_{10} selectivity and i-C_{10} yield. Pt/C-S displayed lower i-C_{10} selectivity and i-C_{10} yield and higher cracking selectivity than Pt/ZS-9 and Pt/ZS-M. This was because C-S had larger SAPO-11

crystallites (310 nm) and smaller mesopore volumes (Table 1), which disfavored diffusion of i-C_{10} intermediates, boosted the cracking side reactions and limited formation of the i-C_{10} products (Wen et al., 2021).

ZS-M prepared by mechanically mixing ZSM-22 and SAPO-11 had large ZSM-22 (680 nm) and SAPO-11 (310 nm) crystallites, which provided long diffusion paths for i-C_{10} intermediates and therefore accelerated the cracking side reactions. Consequently, the corresponding Pt/ZS-M catalyst exhibited a low i-C_{10} yield (Fig. 10a). Compared with ZS-M, ZS-9 had smaller ZSM-22 (490 nm) and SAPO-11 (210 nm) crystallites due to electrostatic repulsions
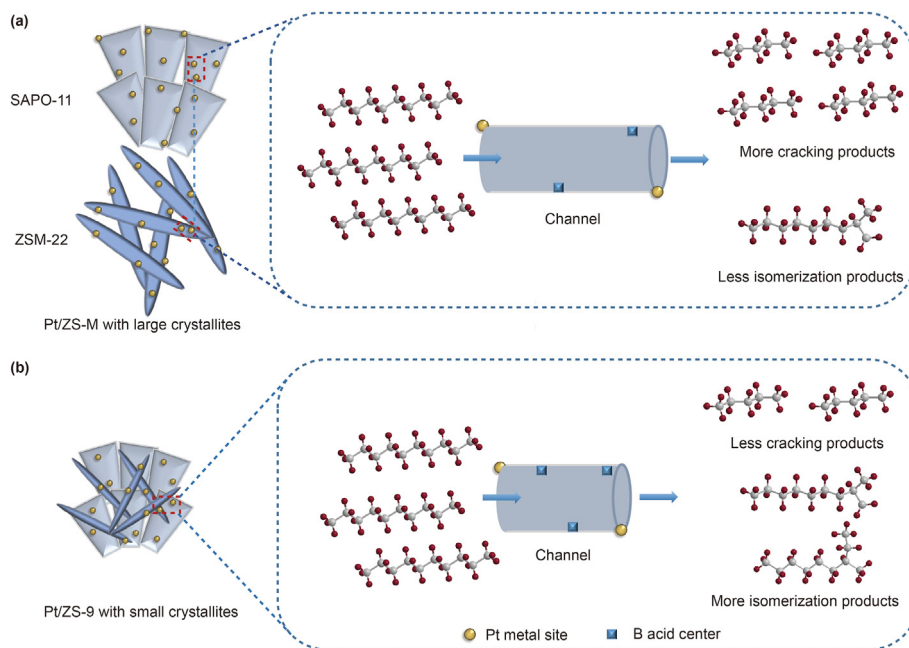
Fig. 10. Reaction paths of n-C_{10} hydroisomerization over Pt/ZS-M (**a**) and Pt/ZS-9 (**b**).

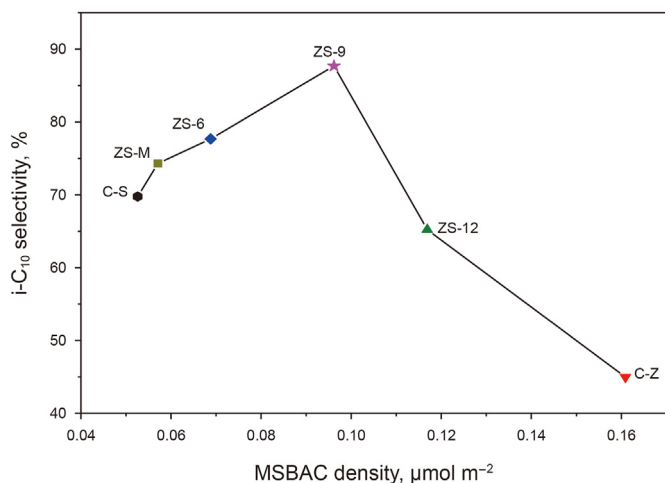**Fig. 11.** i-C_{10} selectivities versus MSBAC densities of the molecular sieves.

between the ZSM-22 precursor and SAPO-11 crystalline nuclei during synthesis, which shortened the diffusion paths of i-C_{10} intermediates (Fig. 10b). In addition, ZS-9 had more MSBAC content (23.0 μmol/g) than ZS-M (12.5 μmol/g), which supplied more active sites for n-C_{10} skeletal isomerizations. Consequently, Pt/ZS-9 showed higher n-C_{10} conversion, higher i-C_{10} selectivity and yield and lower cracking selectivity than Pt/ZS-M.

The relationship between i-C_{10} selectivity and the MSBAC density of molecular sieves was investigated for an n-C_{10} conversion of approximately 93%, and the results are displayed in Fig. 11. The i-C_{10} selectivity increased first and then decreased with increasing MSBAC density. This is because the molecular sieve had a small MSBAC content per unit specific surface area when the MSBAC density was low, which led to a small number of active sites available for skeletal isomerization; thus, the corresponding catalyst displayed a low i-C_{10} selectivity. However, the molecular sieve with high MSBAC density had a large MSBAC content per specific surface area, which accelerated the cracking side reactions but inhibited skeletal isomerizations over the corresponding catalysts.
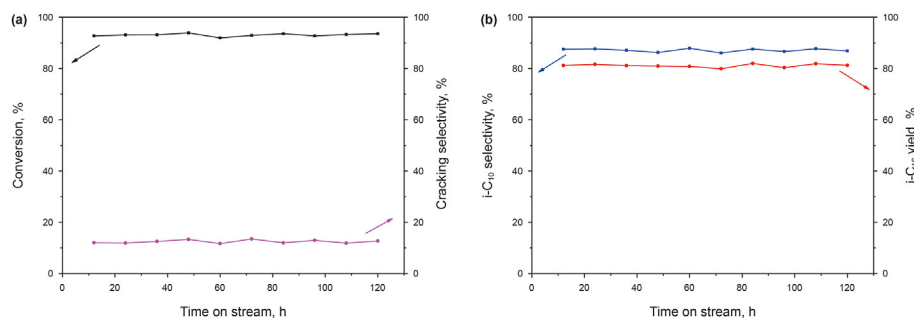

Fig. 12. n-C_{10} conversion and cracking selectivity (**a**), and i-C_{10} selectivity and i-C_{10} yield (**b**) versus reaction time over Pt/ZS-9.

Hence, when the MSBAC density was 9.6×10^{-2} μmol m^{-2}, the corresponding Pt/ZS-9 catalyst exhibited the highest i-C$_{10}$ selectivity (87.7%).

Furthermore, the n-C$_{10}$ hydroisomerization stability for the optimal Pt/ZS-9 catalyst was investigated at 350 °C, 2.0 MPa, 3.0 h^{-1} and $v(H_2)/v(n\text{-}C_{10}) = 400$, and the results are presented in Fig. 12. The n-C$_{10}$ conversion, i-C$_{10}$ selectivity, i-C$_{10}$ yield and cracking selectivity for Pt/ZS-9 were almost constant, showing the excellent stability of Pt/ZS-9 for n-C$_{10}$ hydroisomerization.

4. Conclusions

A series of ZSM-22/SAPO-11 composite molecular sieves were synthesized by adding different amounts of ZSM-22 into the synthetic gel of SAPO-11, and n-C$_{10}$ hydroisomerization over these corresponding catalysts were investigated. When the mass fraction of ZSM-22 in the ZSM-22/SAPO-11 composite was 6.5%, ZSM-22/SAPO-11 (ZS-6) had large crystallites and a low MSBAC content. As the mass fraction of ZSM-22 in ZSM-22/SAPO-11 was increased to 9.4%, ZSM-22/SAPO-11 (ZS-9) presented smaller SAPO-11 (210 nm) and ZSM-22 (490 nm) crystallites and a higher MSBAC content (23.0 μmol/g) than ZS-6. With a further increase of the mass fraction of ZSM-22 in ZSM-22/SAPO-11 to 12.2%, the crystallite sizes of ZSM-22/SAPO-11 were slightly reduced, but the MSBAC content was excessive, resulting in enhancement of cracking side reactions. In contrast to SAPO-11, ZSM-22 and their mechanical mixture, ZS-9 had smaller ZSM-22 and SAPO-11 crystallites and the optimal MSBAC density (9.6×10^{-2} μmol m^{-2}), which enabled its corresponding Pt/ZS-9 catalyst to generate a higher i-C$_{10}$ yield (81.6%), lower cracking selectivity (11.9%) and excellent stability.

Declaration of competing interest

The authors declare that they have no known competing financial interests or personal relationships that could have appeared to influence the work reported in this paper.

Acknowledgement

Appendix A. Supplementary data

Supplementary data to this article can be found online at https://doi.org/10.1016/j.petsci.2023.03.002.

References

Barrett, E.P., Joyner, L.G., Halenda, P.P., 1951. The determination of pore volume and area distributions in porous substances. I. computations from nitrogen isotherms. J. Am. Chem. Soc. 73 (1), 373–380. https://doi.org/10.1021/ja01145a126.

Buchanan, J.S., Santiesteban, J.G., Haag, W.O., 1996. Mechanistic considerations in acid-catalyzed cracking of olefins. J. Catal. 158, 279–287. https://doi.org/10.1006/jcat.1996.0027.

Chi, K.B., Zhao, Z., Tian, Z.J., et al., 2013. Hydroisomerization performance of platinum supported on ZSM-22/ZSM-23 intergrowth zeolite catalyst. Petrol. Sci. 10 (2), 242–250. https://doi.org/10.1007/S12182-013-0273-6.

Claude, M.C., Martens, J.A., et al., 2000. Monomethyl-branching of long n-alkanes in the range from decane to tetracosane on Pt/H-ZSM-22 bifunctional catalyst. J. Catal. 190 (1), 39–48. https://doi.org/10.1006/jcat.1999.2714.

Dai, X.J., Cheng, Y., Si, M., et al., 2022. SAPO-11 molecular sieves synthesized in alcohol-water concentrated gel system with improved acidity, mesoporous volume and hydroisomerization performance. Fuel 314, 123131. https://doi.org/10.1016/j.fuel.2022.123131.

Danilina, N., Krumeich, F., van Bokhoven, J.A., 2010. Hierarchical SAPO-5 catalysts active in acid-catalyzed reactions. J. Catal. 272 (1), 37–43. https://doi.org/10.1016/j.jcat.2010.03.014.

Deldari, H., 2005. Suitable catalysts for hydroisomerization of long-chain normal paraffins. Appl. Catal. Gen. 293, 1–10. https://doi.org/10.1016/j.apcata.2005.07.008.

Duan, C., Zhang, X., Zhou, R., et al., 2013. Comparative studies of ethanol to propylene over HZSM-5/SAPO-34 catalysts prepared by hydrothermal synthesis and physical mixture. Fuel Process. Technol. 108, 31–40. https://doi.org/10.1016/j.fuproc.2012.03.015.

Fan, Y., Lei, D., Shi, G., et al., 2006. Synthesis of ZSM-5/SAPO-11 composite and its application in FCC gasoline hydro-upgrading catalyst. Catal. Today 114 (4), 388–396. https://doi.org/10.1016/j.cattod.2006.02.050.

Feng, Z.L., Wang, W., Wang, Y., et al., 2019. Hydroisomerization of n-decane over the Pd/ZSM-22 bifunctional catalysts: the effects of dynamic and static crystallization to the zeolite. Microporous Mesoporous Mater. 274, 1–8. https://doi.org/10.1016/j.micromeso.2018.07.012.

Gollakota, A.R.K., Volli, V., Munagapati, V.S., et al., 2020. Synthesis of novel ZSM-22 zeolite from taiwanese coal fly ash for the selective separation of rhodamine 6G. J. Mater. Res. Technol. 9 (6), 15381–15393. https://doi.org/10.1016/j.jmrt.2020.10.070.

Guo, L., Bao, X.J., Fan, Y., et al., 2012. Impact of cationic surfactant chain length during SAPO-11 molecular sieve synthesis on structure, acidity, and n-octane isomerization to di-methyl hexanes. J. Catal. 294, 161–170. https://doi.org/10.1016/j.jcat.2012.07.016.

Hao, J., Cheng, D.G., Chen, F.Q., et al., 2021. n-Heptane catalytic cracking on ZSM-5 zeolite nanosheets: effect of nanosheet thickness. Microporous Mesoporous Mater. 310, 110647. https://doi.org/10.1016/j.micromeso.2020.110647.

Hoang, P.H., Nhung, N.T., Dien, L.Q., 2017. Synthesis of mesoporous Cr/ZSM-5 and W-Cr/ZSM-5 zeolite catalysts for oxidation of unsaturated fatty acid. AIP Adv. 7, 105311. https://doi.org/10.1063/1.4986310.

Jaroszewska, K., Fedyna, M., Trawczyński, J., 2019. Hydroisomerization of long-chain n-alkanes over Pt/AlSBA-15+zeolite bimodal catalysts. Appl. Catal. B Environ. 255, 117756. https://doi.org/10.1016/j.apcatb.2019.117756.

Jin, C.L., Ma, B., Zhang, X.W., et al., 2009. Catalytic performance of Pt/HY-β in n-octane hydroisomerization. Petrol. Sci. 6 (3), 299–305. https://doi.org/10.1007/S12182-009-0048-2.

Lippens, B.C., Boer, J.H., 1965. Studies on pore systems in catalysts: V. the t method. J. Catal. 4 (3), 319–323. https://doi.org/10.1016/0021-9517(65)90307-6.

Liu, S.Y., Ren, J., Zhu, S.J., et al., 2015. Synthesis and characterization of the Fe-substituted ZSM-22 zeolite catalyst with high n-dodecane isomerization performance. J. Catal. 330, 485–496. https://doi.org/10.1016/j.jcat.2015.07.027.

Liu, Y.X., Liu, W.R., Lyu, Y.C., et al., 2020. Intra-crystalline mesoporous SAPO-11 prepared by a grinding synthesis method as FCC promoters to increase iso-paraffin of gasoline. Microporous Mesoporous Mater. 305, 110320. https://doi.org/10.1016/j.micromeso.2020.110320.

Lyu, Y.C., Liu, Y.X., He, X., et al., 2018. The regulation of Si distribution and surface acidity of SAPO-11 molecular sieve. Appl. Surf. Sci. 453, 350–357. https://doi.org/10.1016/j.apsusc.2018.05.106.

Lyu, Y.C., Yu, Z.M., Yang, Y., et al., 2019. Metal-acid balance in the in-situ solid synthesized Ni/SAPO-11 catalyst for n-hexane hydroisomerization. Fuel 243, 398–405. https://doi.org/10.1016/j.fuel.2019.01.013.

Lyu, Y.C., Zhan, W.L., Wang, X.X., et al., 2020. Regulation of synergy between metal and acid sites over the Ni-SAPO-11 catalyst for n-hexane hydroisomerization. Fuel 274, 117855. https://doi.org/10.1016/j.fuel.2020.117855.

Oenema, J., Harmel, J., Velez, R.P., et al., 2020. Influence of nanoscale intimacy and zeolite micropore size on the performance of bifunctional catalysts for n-heptane hydroisomerization. ACS Catal. 10 (23), 14245–14257. https://doi.org/10.1021/acscatal.0c03138.

Parry, E.P., 1963. An infrared study of pyridine adsorbed on acidic solids. characterization of surface acidity. J. Catal. 2, 371–379. https://doi.org/10.1016/0021-9517(63)90102-7.

Pieterse, J.A.Z., Veefkind-Reyes, S., Seshan, K., et al., 1999. On the accessibility of acid sites in ferrierite for pyridine. J. Catal. 187, 518–520. https://doi.org/10.1006/jcat.1999.2629.

Qin, B., Zhang, X.W., Zhang, Z.Z., et al., 2011. Synthesis, characterization and catalytic properties of Y-β zeolite composites. Petrol. Sci. 8 (2), 224–228. https://doi.org/10.1007/s12182-011-0139-8.

Wang, X.L., Mei, J.L., Zhao, Z., et al., 2018. Self-assembly of hierarchically porous ZSM-5/SBA-16 with different morphologies and its high isomerization performance for hydrodesulfurization of dibenzothiophene and 4,6-dimethyldibenzothiophene. ACS Catal. 8 (3), 1891–1902. https://doi.org/10.1021/acscatal.7b04147.

Wang, X.Y., Zhang, X.W., Wang, Q.F., 2019. n-Dodecane hydroisomerization over hierarchical ZSM-22 prepared by a dual-protected alkali treatment. Ind. Eng. Chem. Res. 58 (19), 8495–8505. https://doi.org/10.1021/acs.iecr.8b06450.

Wei, C.H., Zhang, G.H., Zhao, L., et al., 2022. Effect of metal-acid balance and textual modifications on hydroisomerization catalysts for n-alkanes with different chain length: a mini-review. Fuel 315, 122809. https://doi.org/10.1016/j.fuel.2021.122809.

Wen, C.L., Wang, X.M., Xu, J.D., et al., 2019. Hierarchical SAPO-11 molecular sieve-based catalysts for enhancing the double-branched hydroisomerization of alkanes. Fuel 225, 115821. https://doi.org/10.1016/j.fuel.2019.115821.

Wen, C.L., Xu, J.D., Wang, X.M., et al., 2020. n-Heptane hydroisomerization over a SO$_4^{2-}$/ZrO$_2$@SAPO-11 composite-based catalyst derived from the growth of UiO-66 on SAPO-11. Energy Fuel. 34 (8), 9498–9508. https://doi.org/10.1021/acs.energyfuels.0c01634.

Wen, C.L., Xu, J.D., Wang, X.M., et al., 2021. n-Nonane hydroisomerization over

hierarchical SAPO-11-based catalysts with sodium dodecylbenzene sulfonate as a dispersant. Petrol. Sci. 18, 654–666. https://doi.org/10.1007/s12182-021-00544-3.

Yu, G., Chen, X.Q., Xue, W.J., et al., 2020. Melting-assisted solvent-free synthesis of SAPO-11 for improving the hydroisomerization performance of n-dodecane. Chin. J. Catal. 41 (4), 622–630. https://doi.org/10.1016/S1872-2067(19)63466-2.

Yu, G., Qiu, M.H., Wang, T., et al., 2021. Optimization of the pore structure and acidity of SAPO-11 for highly efficient hydroisomerization on the long-chain alkane. Microporous Mesoporous Mater. 320, 111076. https://doi.org/10.1016/j.micromeso.2021.111076.

Zhai, M., Wu, W.X., Xing, E.H., et al., 2022. Generating TON zeolites with reduced [001] length through combined mechanochemical bead-milling and porogen-directed recrystallization with enhanced catalytic property in hydroisomerization. Chem. Eng. J. 440, 135874. https://doi.org/10.1016/j.cej.2022.135874.

Zhan, W.L., Lyu, Y.C., Liu, X.M., et al., 2022. The direct synthesis of Ni/SAPO-11 hydroisomerization catalyst via a novel two-step crystallization strategy. Petrol. Sci. 19 (5), 2448–2459. https://doi.org/10.1016/j.petsci.2022.01.014.

Zhang, P., Liu, H.Y., Yue, Y., et al., 2018. Direct synthesis of hierarchical SAPO-11 molecular sieve with enhanced hydroisomerization performance. Fuel Process. Technol. 179, 72–85. https://doi.org/10.1016/j.fuproc.2018.06.012.

Zhang, X., Wang, J.W., Zhong, J., et al., 2008. Characterization and catalytic performance of SAPO-11/Hβ composite molecular sieve compared with the mechanical mixture. Microporous Mesoporous Mater. 108 (1–3), 13–21. https://doi.org/10.1016/j.micromeso.2007.03.022.

Zhang, Y.D., Liu, D., Men, Z.W., et al., 2019. Hydroisomerization of n-dodecane over bi-porous Pt-containing bifunctional catalysts: effects of alkene intermediates' journey distances within the zeolite micropores. Fuel 236, 428–436. https://doi.org/10.1016/j.fuel.2018.09.017.

Zheng, J.J., Wang, G.S., Pan, M., et al., 2015. Hierarchical core–shell zeolite composite ZSM-5@SAPO-34 fabricated by using ZSM-5 as the nutrients for the growth of SAPO-34. Microporous Mesoporous Mater. 206, 114–120. https://doi.org/10.1016/j.micromeso.2014.12.011.

Zhou, J., Liu, Z.C., Wu, W., et al., 2011. Direct synthetic strategy of mesoporous ZSM-5 zeolites by using conventional block copolymer templates and the improved catalytic properties. ACS Catal. 1, 287–291. https://doi.org/10.1021/cs1000976.

Zhu, S.J., Liu, S.Y., Zhang, H.K., et al., 2014. Investigation of synthesis and hydroisomerization performance of SAPO-11/Beta composite molecular sieve. China Journal of Catalysis 35 (10), 1676–1686. https://doi.org/10.1016/S1872-2067(14)60133-9.